RSC Advances

PAPER

Cite this: *RSC Adv.*, 2024, **14**, 4568

Integration of a Cu_2O/ZnO heterojunction and Ag@SiO_2 into a photoanode for enhanced solar water oxidation†

Xuyang Zeng,[ab] Qianyu Gao,[ab] Peilin Song,[b] Xinru Zhang,[b] Jiaying Xie,[b] Qingwen Dong,[b] Junjie Qi,[b] Xiu-Shuang Xing *[b] and Jimin Du*[ab]

Photoelectrochemical water splitting (PEC-WS) has attracted considerable attention owing to its low energy consumption and sustainable nature. Constructing semiconductor heterojunctions with controllable band structure can effectively facilitate photogenerated carrier separation. In this study, a FTO/ZnO/Cu_2O/Ag@SiO_2 photoanode with a Cu_2O/ZnO p–n heterojunction and Ag@SiO_2 nanoparticles is constructed to investigate its PEC-WS performance. Compared with a bare ZnO photoanode, the photocurrent density of the FTO/ZnO/Cu_2O/Ag@SiO_2 photoanode (0.77 mA cm^{-2}) at 1.23 V_{RHE} exhibits an increment of 88%, and a cathodic shift of 0.1 V for the on-set potential (0.4 V_{RHE}). Detailed photoelectrochemical analyses reveal that the Cu_2O/ZnO p–n heterojunction formed between Cu_2O and ZnO can effectively promote photogenerated carrier separation. The surface plasmonic effect of the Ag@SiO_2 nanoparticles can further promote the photogenerated carrier transfer efficiency, which synergistically improves the PEC-WS performance.

Received 13th November 2023
Accepted 25th January 2024

DOI: 10.1039/d3ra07738a

rsc.li/rsc-advances

Introduction

With rapid technological and industrial advances, environmental pollution and the energy crisis have become urgent issues. Developing clean and sustainable energy is crucial to alleviate this crisis.[1] Photoelectrochemical water splitting (PEC-WS) has attracted extensive research attention because it can be a low-cost, renewable and environmentally friendly method for hydrogen production.[2,3] Various metal oxide semiconductor materials, such as TiO_2,[4] ZnO,[5] α-Fe_2O_3,[6] and $BiVO_4$,[7] have been widely applied to investigate their PEC-WS performances. Among these, ZnO is an n-type semiconductor with a band gap energy of ~3.3 eV, which exhibits a suitable band position and high electron mobility, and can be considered as one of the popular semiconductor materials in the photocatalysis field.[8–11] However, its further applications are limited to the rapid recombination of photogenerated carriers and low utilization of visible light.[12]

Various methods, such as metal doping, surface catalysts, and heterojunction construction, are applied to improve the photoelectric conversion efficiency of ZnO.[13–15] The construction of heterojunctions is one of the effective methods to improve PEC-WS performance and also attracts widespread attention.[16] Z-type heterojunctions can provide a stable internal electric field between semiconductors and accelerate the migration of photogenerated carrier, which are preferred over general heterojunctions.[17–19] For instance, Li *et al.* prepared a semiconductor with a ZnO/ZnS heterojunction by ion exchange sulfidation treatment, and found the photocurrent density was 1.35 times that of the bare ZnO photoanode at 1.23 V_{RHE}.[20] Maity *et al.* synthesized n-ZnO/p-$ZnCo_2O_4$ photoanodes with heterojunctions, in which the introduction of $ZnCo_2O_4$ decreased surface defects, inhibited the recombination of photogenerated carrier, and increased the photocurrent density of ZnO photoanodes.[21,22]

In this study, ZnO photoanodes with nanosheet-like structures are prepared by a hydrothermal method, where Cu_2O is introduced on the surface of ZnO to construct a Cu_2O/ZnO p–n heterojunction structure. The FTO/ZnO/Cu_2O/Ag@SiO_2 photoanode exhibits a maximum photocurrent density of 0.77 mA cm^{-2} at 1.23 V_{RHE}, which increases by 88% compared with the bare FTO/ZnO photoanode. This is mainly attributed to the p–n heterojunction formed between Cu_2O and ZnO, which effectively promotes the separation and transfer efficiency of photogenerated carrier. The introduction of Ag@SiO_2 catalyst further increases the transfer efficiency of photogenerated electrons and holes *via* the surface plasmonic effect.

[a]*College of Chemistry, Zhengzhou University, Zhengzhou 450000, P. R. China. E-mail: djm@iccas.ac.cn*

[b]*Henan Key Laboratory of New Optoelectronic Functional Materials, College of Chemistry and Chemical Engineering, Anyang Normal University, Anyang 455000, P. R. China. E-mail: xsxing0621@163.com*

† Electronic supplementary information (ESI) available. See DOI: https://doi.org/10.1039/d3ra07738a

Experimental

Preparing FTO/ZnO photoanodes

The ingredients and reagents used herein were purchased and used directly without additional purification. FTO conductive glass was ultrasonically cleaned with acetone, ethanol, and deionized water for 15 min, successively. The FTO substrate was obliquely placed in a Teflon reactor, where its conductive side was facing down. ZnOOH films were prepared using the hydrothermal method: 0.4998 g $Zn(NO_3)_2$ and 0.5043 g urea were dissolved in 60 mL distilled water. This solution was poured into the Teflon reactor and heated in an oven for 7 h at 100 °C. A white ZnOOH film was clearly observed on the FTO glass, and it was labeled as FTO/ZnOOH. This was further annealed at 500 °C for 2 h to prepare the FTO/ZnO photoanode.

Preparing FTO/ZnO/Cu_2O nanorod arrays

Copper sulfate (3.1922 g) and sodium thiosulfate (19.85 g) were separately dissolved in 20 mL and 80 mL of distilled water, respectively. Then, they were placed ultrasonically together for 15 min to obtain a mixed solution. Sodium hydroxide (2 g) was dissolved in 100 mL distilled water. The prepared FTO/ZnO nanorods were immersed in the above mixed solution for 2 s, distilled water for 30 s, an aqueous NaOH solution at 70 °C for 2 s, and finally distilled water for 30 s. The above deposition reaction process constituted one cycle. FTO/ZnO nanorods were treated through one, two and three cycles, and denoted as FTO/ZnO/Cu_2O-1, FTO/ZnO/Cu_2O-2, and FTO/ZnO/Cu_2O-3, respectively. Because of the optimal photoelectrochemical conversion for FTO/ZnO/Cu_2O-2 photoanode, the following modifications with Ag and Ag@SiO_2 were all based on it. Hereafter, the FTO/ZnO/Cu_2O-2 photoanode was also denoted as the FTO/ZnO/Cu_2O photoanode.

Preparing FTO/ZnO/Cu_2O/Ag and FTO/ZnO/Cu_2O/Ag@SiO_2

A mixed silver nitrate (13.25 mmol, 200 mL) and sodium citrate (100 mmol, 1.94 mL) aqueous solution were boiled for 15 min, and cooled to 25 °C to obtain a silver colloidal solution. The silver colloidal solution was centrifuged at 1000 rpm and then washed sequentially with deionized water and ethanol.[22] Finally, the prepared AgNPs and ethanol were dispersed on FTO/ZnO/Cu_2O to obtain the FTO/ZnO/Cu_2O/Ag photoanode.

Furthermore, 25 mL of an ethanol solution containing AgNPs was diluted with ethanol to obtain a 100 mL solution. Then 3 mL of ammonia was added to this solution, and ultrasonicated for 30 min. 10 μL of tetraethyl orthosilicate was added to the above mixed solution, stirred at 30 °C, centrifuged for 10 min to obtain Ag@SiO_2-NPs, and finally washed in turn with deionized water and ethanol.[22] FTO/ZnO/Cu_2O/Ag@SiO_2 was obtained by dispersing Ag@SiO_2-NPs and ethanol in FTO/ZnO/Cu_2O (Scheme 1).

Structure characterization

The surface morphology of ZnO photoanodes was investigated using field-emission scanning electron microscopy (SEM, Quanta 400 FEG and Hitachi S4800), and the micromorphology and elemental composition were characterized using transmission electron microscopy (TEM, FEI Talos F200X) coupled with elements line scanning and energy-dispersive X-ray spectroscopy (EDS). X-ray diffraction (XRD) spectra were recorded using X'Pert Pro MPD (Cu $K\alpha$ radiation). X-ray photoelectron spectroscopy (XPS) was performed on a Thermo ESCALAB 250Xi spectrometer to analyze the surface chemical state and elemental composition of photoanodes. UV-vis spectra were analyzed using UV 3600 Shimadzu.

PEC-WS measurement

Photoelectrochemical measurements were performed on an electrochemical workstation (CHI 660E) with a three-electrode test system (*i.e.*, the prepared ZnO photoanode as the working electrode, Ag/AgCl as the reference electrode, and Pt as the counter electrode). The electrolyte was a 1.0 M NaOH aqueous solution. A simulated sunlight (CEL-HXF3-T3), with a normal power density of 100 mW cm^{-2} and an AM 1.5 G filter, was selected as the light source. Photocurrent density–voltage (J–V) curves were measured from negative potential to positive potential with a sweep speed of 20 mV s^{-1}. Mott–Schottky plots were measured at 1 kHz under dark conditions. Electrochemical impedance spectroscopy (EIS) was conducted under simulated sunlight at 1.23 V_{RHE} from 0.1 Hz to 100 kHz.

Results and discussion

The SEM images show that the ZnO film composes of nanosheets with ~5 nm thickness (Fig. 1a and b). A few Cu_2O nanoparticles grow on the surface of FTO/ZnO photoanode, and the thickness of Cu_2O nanoparticles increases with the increased deposition circles (Fig. S1†). The ZnO film maintains

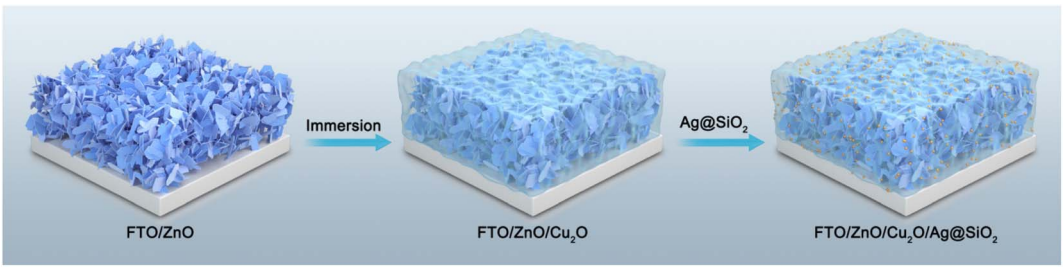

Scheme 1 The schematic preparation procedure of FTO/ZnO/Cu_2O/Ag@SiO_2 photoanode.

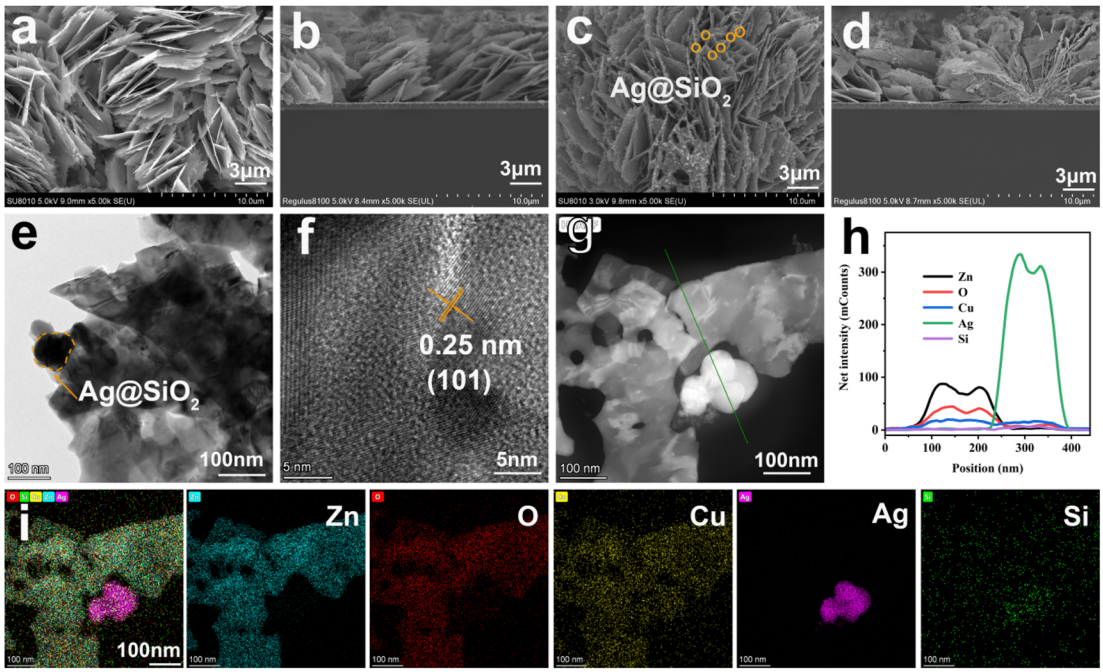

Fig. 1 SEM images of FTO/ZnO (a and b) and FTO/ZnO/Cu_2O/Ag@SiO_2 (c and d); (a and c are the top-view images, b and d are the cross-sectional images); (e) TEM, (f) HR-TEM, (g-h) elements linear scanning images of FTO/ZnO/Cu_2O/Ag@SiO_2; (i) EDS elements mapping images of FTO/ZnO/Cu_2O/Ag@SiO_2 photoanodes.

the nanosheet shape after the introduction of Cu_2O. The characterization peak of ZnO in the XRD spectra keeps almost unchanged (Fig. S2†), indicating that the introduction of Cu_2O has no effect on the ZnO film. The ZnO photoanode modified by Cu_2O exhibits an obvious UV-vis absorbance enhancement at 250∼400 nm, where the FTO/ZnO/Cu_2O-2 photoanode possesses the best light absorption capacity (Fig. S3†).

As shown in the SEM images of Fig. 1c and d, the FTO/ZnO and FTO/ZnO/Cu_2O/Ag@SiO_2 photoanodes all possess a similar nanosheet-like structure, which are closely arranged. This structural character of vertical nanosheets provides favorable bars for the formation of p–n heterojunctions. Many Ag@SiO_2 nanoparticles are accumulated on the surface of the FTO/ZnO/Cu_2O photoanode with a thickness of ∼5 nm (Fig. 1c). TEM is conducted to investigate the morphological changes in the photoanodes after introducing Ag@SiO_2 catalysts (Fig. 1e). The inter-planar distances of 0.25 nm in the shell region match well with the lattice fringes of (101) planes of ZnO (Fig. 1f). ZnO is presented as a nanosheet with a diameter of ∼50 nm modified with Cu_2O and Ag@SiO_2 nanoparticles. EDS data proves the successful introduction of Ag@SiO_2 nanoparticles on the surface of FTO/ZnO/Cu_2O photoanode (Fig. 1g–i). XRD patterns show that the peak positions of FTO/ZnO/Cu_2O/Ag and FTO/ZnO/Cu_2O/Ag@SiO_2 photoanodes are almost the same as that of the pure ZnO photoanode (Fig. S4†), indicating that the introduction of Ag and Ag@SiO_2 nanoparticles cannot cause the phase transition of ZnO photoanodes.[23] In the UV-vis absorption spectra, the absorption edge of each photoanode is ∼400 nm (Fig. S5†). The absorbance intensities of FTO/ZnO/Cu_2O/Ag and FTO/ZnO/Cu_2O/Ag@SiO_2 photoanodes are all stronger than that of the FTO/ZnO photoanode, which can be attributed to the formation of a heterojunction in the interface of ZnO and Cu_2O and the introduced Ag and Ag@SiO_2 catalysts.[24]

XPS is used for surface chemical state and elemental analyses, which proves the existence of elemental Zn, Cu, O, Ag, and Si in the FTO/ZnO/Cu_2O/Ag@SiO_2 photoanode (Fig. S6†). Zn 2p has two main peaks at 1022.1 eV and 1045 eV (Fig. 2a). Spin orbital splitting is also observed in Zn 2p signals, demonstrating the presence of Zn^{2+} in ZnO.[25] The O 1s spectrum mainly consists of two peaks of 531.8 eV (oxygen defect) and 530.3 eV (lattice oxygen). The oxygen vacancy intensity of FTO/ZnO/Cu_2O/Ag photoanode becomes slightly lower, indicating fewer surface defects. The lattice oxygen intensity of FTO/ZnO/Cu_2O/Ag@SiO_2 photoanode is relatively higher, indicating that its surface crystallinity is excellent. After introducing the Cu_2O and Ag@SiO_2 catalysts, the O_v peak moves in a lower binding energy, which is conducive to carrier transfer (Fig. 2b).[26] The ∼933.7 eV and ∼953.4 eV of Cu 2p can be attributed to Cu $2p_{3/2}$ and Cu $2p_{1/2}$, indicating the presence of Cu_2O in the photoanodes (Fig. 2c).[27,28] The two peaks of Ag $3d_{1/2}$ (∼373.9 eV) and Ag $3d_{3/2}$ (∼367.8 eV) also further prove the presence of elemental Ag (Fig. 2d).[29] The XRD patterns are conducted to recognize the phase of ZnO, Cu_2O, Ag and SiO_2 in the FTO/ZnO/Cu_2O/Ag@SiO_2 photoanode, but the Cu_2O and Ag@SiO_2 films are too thin to find their characteristic peaks. The presence of Cu_2O and Ag@SiO_2 are proved mainly by XPS and elemental analysis.[30]

The linear scanning voltammetry, transient photocurrent curves, EIS, and Mott–Schottky measurements are conducted to

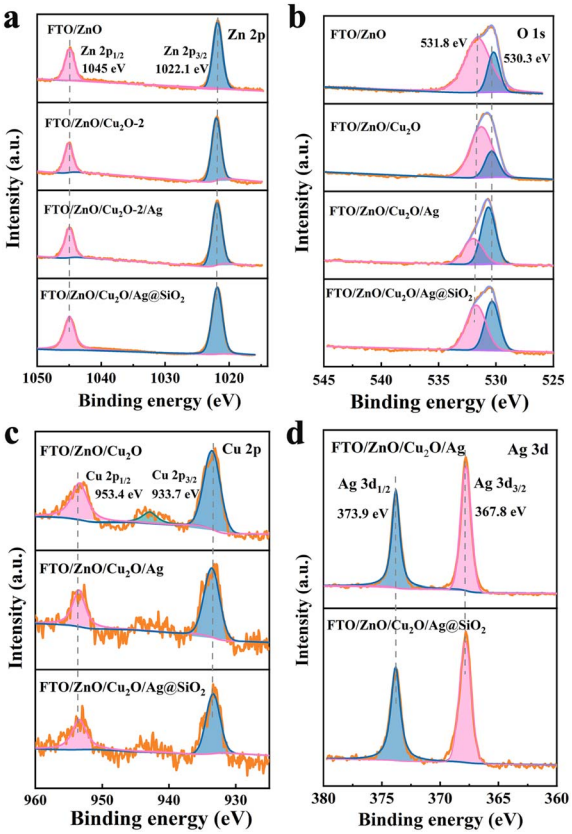

Fig. 2 The XPS spectra of (a) Zn 2p, (b) O 1s in FTO/ZnO, FTO/ZnO/Cu_2O, FTO/ZnO/Cu_2O/Ag and FTO/ZnO/Cu_2O/Ag@SiO_2 photoanodes. The XPS spectra of (c) Cu 2p in FTO/ZnO/Cu_2O, FTO/ZnO/Cu_2O/Ag and FTO/ZnO/Cu_2O/Ag@SiO_2 photoanodes. The XPS spectra of (d) Ag 3d in FTO/ZnO/Cu_2O/Ag and FTO/ZnO/Cu_2O/Ag@SiO_2 photoanodes.

study the effect of Cu_2O and deposition circle on the separation and transfer efficiency of photogenerated carrier in the ZnO photoanodes (Fig. 3). *J–V* curves are measured using linear scanning voltammetry (Fig. 3a). The photocurrent density of ZnO photoanodes modified with Cu_2O is larger than that of the FTO/ZnO photoanode, where the photocurrent density first increases and then decreases with the deposition circles increases. The small peak at 0.4 V_{RHE} may be caused by the reaction between the ZnO film and NaOH solution, in which the photocurrent density increases much slow with the increasing potential. When the applied potential is far below 0.4 V_{RHE}, the water-oxidation dynamics limits the photocurrent density. While close to or over 0.4 V_{RHE}, the photogenerated carrier can be efficiently separated and transferring into the electrolyte. The enhancement of photocurrent density is significantly slower as the applied potential is greater than 0.8 V_{RHE}, which is possibly due to the limitation of light absorbance for ZnO photoanodes.[24] The excessively low photogenerated carrier separation efficiency may enlarge the effect of side reaction in the *J–V* curve. The FTO/ZnO/Cu_2O-2 photoanode exhibits the best photocurrent density of 0.67 mA cm^{-2} at 1.23 V_{RHE}. Thus, the introduction of p–n heterojunction can effectively improve the photocurrent density of ZnO photoanode to achieve a better

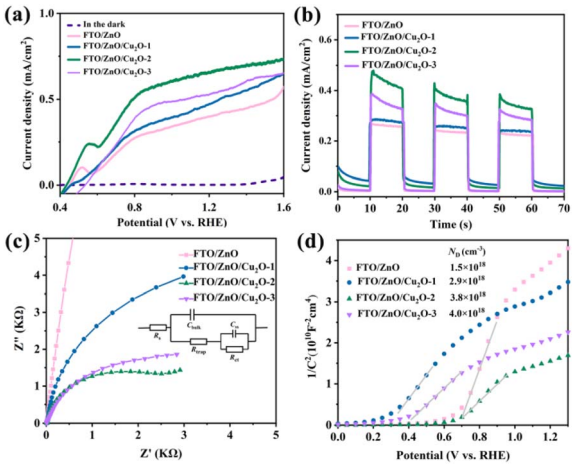

Fig. 3 The (a) *J–V* curves, (b) Transient photocurrent density curves, (c) Nyquist plots at 1.23 V_{RHE} and (d) Mott–Schottky plots of FTO/ZnO, FTO/ZnO/Cu_2O-1, FTO/ZnO/Cu_2O-2 and FTO/ZnO/Cu_2O-3 photoanodes.

PEC-WS performance.[31] The change trends of transient photocurrent density for FTO/ZnO, FTO/ZnO/Cu_2O-1, FTO/ZnO/Cu_2O-2, and FTO/ZnO/Cu_2O-3 photoanodes are the same as those of the corresponding *J–V* curves (Fig. 3b), proving that the heterojunction formed between ZnO and Cu_2O can hinder the recombination rate of photogenerated carrier.[32] An equivalent circuit is shown in Fig. 3c, where R_s, R_{trap}, and R_{CT} represent the series resistance, capture resistance on the surface, and transfer resistance from the surface to the electrolyte, respectively. The arc radii of photoanodes modified with Cu_2O are smaller than that of the pure ZnO photoanode, where the FTO/ZnO/Cu_2O-2 photoanode exhibits the smallest arc radius. This implies that the ZnO/Cu_2O p–n heterojunction can effectively decrease the transport resistance to further promote charge transfer.[33] Fig. 3d reveals four different Mott–Schottky curves, where a greater slope implies a smaller donor density. The fitting results show that the slope of FTO/ZnO/Cu_2O-2 is the smallest, indicating its largest donor density. These results demonstrate that the FTO/ZnO/Cu_2O-2 photoanode possesses the optimal PEC-WS performance. To better study the photoelectrochemical properties of ZnO photoanodes, FTO/ZnO/Cu_2O-2 is denoted as FTO/ZnO/Cu_2O photoanode in the following.

To further improve the PEC-WS performance of FTO/ZnO/Cu_2O photoanode, Ag and Ag@SiO_2 nanoparticles are introduced to modify its surface. As shown in Fig. 4a, the photocurrent densities of FTO/ZnO/Cu_2O/Ag and FTO/ZnO/Cu_2O/Ag@SiO_2 photoanodes at 1.23 V_{RHE} are significantly greater than that of FTO/ZnO/Cu_2O photoanode. The FTO/ZnO/Cu_2O/Ag@SiO_2 photoanode exhibits the largest photocurrent density of 0.77 mA cm^{-2} at 1.23 V_{RHE}, which is 1.15 times that of FTO/ZnO/Cu_2O photoanode, which is mainly due to that the surface plasmonic effect of Ag@SiO_2 nanoparticles effectively promote photogenerated carrier transfer.[34] When Ag@SiO_2 plasmonic micitons metal nanostructures are adjacent to ZnO semiconductors to form composite plasmonic micitons metal/semiconductor photocatalysts, this relaxation process will be

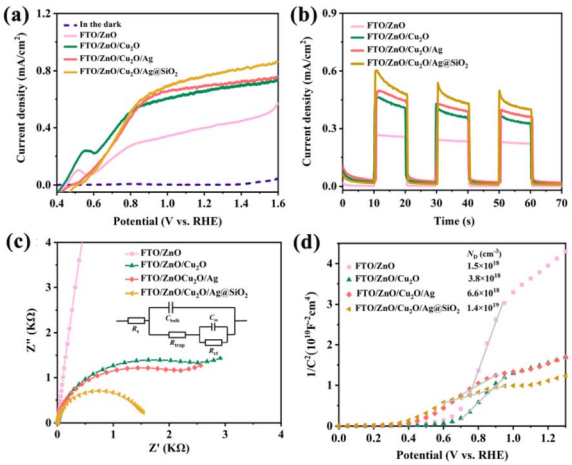

Fig. 4 The (a) *J–V* curves, (b) transient photocurrent density curves, (c) Nyquist plots at 1.23 V_{RHE} and (d) Mott–Schottky plots of FTO/ZnO, FTO/ZnO/Cu_2O, FTO/ZnO/Cu_2O/Ag and FTO/ZnO/Cu_2O/Ag@SiO_2 photoanodes.

effectively extended. This is mainly due to that the plasmon-excited thermal electrons can be injected into the semiconductor from the nanostructures to further enhance the photocatalytic performance.[35–37]

A comparison of PEC-WS performances between ZnO photoanodes in the related literature and our present FTO/TiO_2/Cu_2O/Ag@SiO_2 photoanode is shown in Table S1,† indicating that it possesses a relative better PEC-WS performance.[38–41] The comparison result also indicates that the Cu_2O film and Ag@SiO_2 catalysts possess a remarkable catalytic effect on the PEC-WS performance of ZnO photoanodes.[42–44] The photostability data of FTO/ZnO/Cu_2O/Ag@SiO_2 photoanode are provided. The photocurrent shows a drastic decrease at the beginning illumination and an increasing decay with continuous illumination (Fig. S7†). After the stability testing, *J–t* curves show a certain decrease in photocurrent density due to the gradual corrosion of Cu_2O and Ag@SiO_2 from the ZnO photoanode (Fig. S8 and S9†). The corresponding XRD patterns (Fig. S10†) prove that there is no obvious change in chemical structure in the ZnO photoanode before and after the stability test.[45]

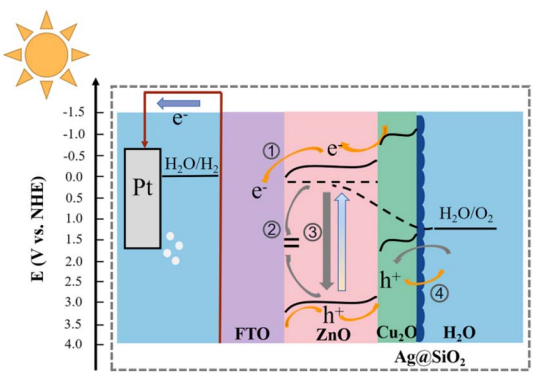

Fig. 5 Schematic diagram of carrier transports in FTO/ZnO/Cu_2O/Ag@SiO_2 photoanode.

The variation tendencies of transient current density for FTO/ZnO/Cu_2O, FTO/ZnO/Cu_2O/Ag, and FTO/ZnO/Cu_2O/Ag@SiO_2 photoanodes are consistent with those of the *J–V* curves (Fig. 4b).

The transient photocurrent densities of FTO/ZnO/Cu_2O/Ag and FTO/ZnO/Cu_2O/Ag@SiO_2 decrease significantly because of the oxidation of Ag and Ag@SiO_2 during the photoelectrochemical process.[45] As shown in Fig. 4c, the FTO/ZnO/Cu_2O/Ag@SiO_2 photoanode possesses the smallest arc radius, indicating that the introduction of Ag@SiO_2 catalyst can decrease the charge transfer resistance to accelerate the photogenerated carrier transfer.[46] The four different Mott–Schottky curves in Fig. 4d also demonstrate that the FTO/ZnO/Cu_2O/Ag@SiO_2 photoanode has the smallest slope and highest donor density, implying that the introduction of Ag@SiO_2 catalyst improves the photogenerated carrier transport.[47]

Fig. 5 shows a schematic diagram of carrier transport for the FTO/ZnO/Cu_2O/Ag@SiO_2 photoanode in the PEC-WS process. Upon illumination, the photogenerated holes in the Cu_2O move toward the Cu_2O/electrolyte interface and oxidize water to produce oxygen, and the photogenerated electrons in ZnO move toward to Pt counter electrode by circuit connection to produce hydrogen. The band alignment characteristics at the p–n junction between ZnO and Cu_2O can produce photovoltage, and help to reduce the loss of holes in the Cu_2O. The p–n heterojunction can improve the electron separation from the hole, and the Ag@SiO_2 nanoparticles at the surface can suppress the surface recombination and also facilitate the oxidation reaction.[48] The carrier transport of ZnO photoanode contains four processes: (1) photogenerated electron transfer, (2) bottom surface recombination, (3) bulk recombination, and (4) photogenerated hole transfer.[49,50] After introducing the Cu_2O and Ag@SiO_2 catalysts on the surface of ZnO, the total amount of photogenerated carrier remains almost unchanged.[51,52] The photogenerated electrons and holes of FTO/ZnO/Cu_2O/Ag@SiO_2 photoanode are excited when irradiated. Based on the formation of p–n heterojunctions and Ag@SiO_2 nanoparticles, the photogeneration of electrons improves (1) due to the decreased bottom surface recombination (2), the bulk recombination process was significantly weakened due to the improved conductivity (3), the surface transfer efficiency of photogenerated carrier is improved based on the internal electric field and surface catalysis (4).

Conclusions

In this study, a serial of nanosheet-like FTO/ZnO photoanodes are prepared modified with the Cu_2O and Ag@SiO_2 nanoparticles, where a Cu_2O/ZnO p–n heterojunction is formed on the surface of ZnO to promote photogenerated carrier transfer. The photocurrent density of FTO/ZnO/Cu_2O/Ag@SiO_2 is 0.77 mA cm^{-2} at 1.23 V_{RHE}, which is 1.88 times that of the pure ZnO photoanode. Photoelectrochemical analyses demonstrate that a p–n heterojunction formed between ZnO and Cu_2O can effectively improve the photogenerated carrier transfer efficiency. The introduction of Cu_2O and Ag@SiO_2 catalysts significantly enhances the absorbance intensity of FTO/ZnO/

Cu_2O/Ag@SiO_2 photoanode. The p–n heterojunction between ZnO and Cu_2O and plasmonic effect of Ag@SiO_2 nanoparticles synergistically promote the transfer efficiency of photogenerated carrier. This study provides an insight for designing the nanostructures of semiconductor materials for high PEC-WS performances.

Conflicts of interest

There are no conflicts to declare.

Acknowledgements

This work was supported by the National Natural Science Foundation of China (22001011), the Teaching Reform Research and Practice Project of Higher Education in Henan Province (2021SJGLX493) and the Scientific Research and Innovation Talent Project of Anyang Normal University (2023AYSYKYCXRC04).

Notes and references

1 X.-S. Xing, X. Zeng, Z. Zhou, Z. M. El-Bahy, M. H. Helal, Q. Gao, H. Algadi, P. Song, X. Liu, X. Zhang and J. Du, *Adv. Compos. Hybrid Mater.*, 2023, **6**, 194.
2 S. Chandrasekaran, L. Yao, L. Deng, C. Bowen, Y. Zhang, S. Chen, Z. Lin, F. Peng and P. Zhang, *Chem. Soc. Rev.*, 2019, **48**, 4178–4280.
3 S. Chandrasekaran, C. Bowen, P. Zhang, Z. Li, Q. Yuan, X. Ren and L. Deng, *J. Mater. Chem. A*, 2018, **6**, 11078–11104.
4 N. D. Quang, P. C. Van, D. D. Le, S. Majumder, N. D. Chinh, J.-R. Jeong, C. Kim and D. Kim, *Appl. Surf. Sci.*, 2021, **558**, 149898.
5 Z. Yu, H. Gong, J. Xu, Y. Li, Y. Zeng, X. Liu and D. Tang, *Anal. Chem.*, 2022, **94**, 3418–3426.
6 D. Chen, Z. Liu, Z. Guo, W. Yan and M. Ruan, *Chem. Eng. J.*, 2020, **381**, 122655.
7 P. Peerakiatkhajohn, J.-H. Yun, T. Butburee, M. Lyu, C. Takoon and S. Thaweesak, *RSC Adv.*, 2023, **13**, 18974–18982.
8 X.-S. Xing, Z. Zhou, P. Song, X. Song, X. Ren, D. Zhang, X. Zeng, Y. Guo and J. Du, *Dalton Trans.*, 2023, **52**, 12308–12317.
9 X. Xing, X. Zeng, Z. Zhou, X. Song, X. Jing, M. Yuan, X. Xu, X. Ren and J. Du, *Dalton Trans.*, 2023, **52**, 11203–11212.
10 X. Ren, X. Zeng, Y. Wang, X. Liu, A. Li, X.-S. Xing and J. Du, *ChemistrySelect*, 2022, **7**, e202203608.
11 D. Bu, M. Batmunkh, Y. Zhang, Y. Li, B. Qian, Y. Lan, X. Hou, S. Li, B. Jia, X.-M. Song and T. Ma, *Chem. Eng. J.*, 2022, **433**, 133559.
12 Z. Zhou, S. Wu, C. Xiao, L. Li, W. Shao, H. Ding, L. Wen and X. Li, *Dalton Trans.*, 2019, **48**, 15151–15159.
13 Z. Hu, R. Wang, C. Han and R. Chen, *J. Colloid Interface Sci.*, 2022, **628**, 946–954.
14 T. Tanaka, R. Tsutsumi, T. Yoshinaga, T. Sonoyama, K. Saito, Q. Guo and S. Ikeda, *RSC Adv.*, 2023, **13**, 575–580.
15 W. He, L. Liu, T. Ma, H. Han, J. Zhu, Y. Liu, Z. Fang, Z. Yang and K. Guo, *Appl. Catal., B*, 2022, **306**, 121107.
16 L. Zhang, G. Wang, X. Hao, Z. Jin and Y. Wang, *Chem. Eng. J.*, 2020, **395**, 125113.
17 Z. Zhou, F. Wang, P. Liang, L. Yang, Y. Yu, L. Li, Y. Guo and S. Wu, *ACS Appl. Energy Mater.*, 2022, **5**, 8999–9008.
18 Z. Zhou, Y. Liang, X.-S. Xing, K. Zhang, Y. Niu, L. Yang, F. Wang, Z. Guo, H. Song and S. Wu, *Adv. Compos. Hybrid Mater.*, 2023, **6**, 94.
19 A. P. Sulaeman, R. A. Pratama, U. Pratomo, Irkham, A. S. Matharu and I. Primadona, *RSC Adv.*, 2023, **13**, 18396–18403.
20 C. Li, S. Chen, Y. Wang and Z. Hou, *Int. J. Hydrogen Energy*, 2019, **44**, 25416–25427.
21 D. Maity, K. Karmakar, D. Pal, S. Saha, G. G. Khan and K. Mandal, *ACS Appl. Energy Mater.*, 2021, **4**, 11599–11608.
22 X. Gao, S. Wu, J. Yan, X. Zhai and X. Li, *ACS Appl. Mater. Interfaces*, 2016, **8**, 30072–30078.
23 R. Marschall and L. Wang, *Catal. Today*, 2014, **225**, 111–135.
24 Z. Zhou, Y. Wang, L. Li, L. Yang, Y. Niu, Y. Yu, Y. Guo and S. Wu, *J. Mater. Chem. A*, 2022, **10**, 8546–8555.
25 H. Li, J. Liu, C. Wang, H. Yang and X. Xue, *Vacuum*, 2022, **199**, 110891.
26 S. Yusan, A. Bampaiti, S. Aytas, S. Erenturk and M. A. A. Aslani, *Ceram. Int.*, 2016, **42**, 2158–2163.
27 Y. Li and K. Luo, *RSC Adv.*, 2019, **9**, 8350–8354.
28 E. Mustafa, E. A. Dawi, Z. H. Ibupoto, A. M. M. Ibrahim, A. Elsukova, X. Liu, A. Tahira, R. E. Adam, M. Willander and O. Nur, *RSC Adv.*, 2023, **13**, 11297–11310.
29 T. Narkbuakaem, S. Sattayaporn, N. Asito and P. Sujardworakun, *Appl. Surf. Sci.*, 2022, **573**, 151617.
30 H. Li, H. Liu, F. Wang, G. Li, X. Wang and Z. Tang, *Nano Res.*, 2022, **15**, 5824–5830.
31 B. Wu and N. Zheng, *Nano Today*, 2013, **8**, 168–197.
32 X. Fang, X. Zhao, W. Fang, C. Chen and N. Zheng, *Nanoscale*, 2013, **5**, 2205–2218.
33 Z. Wang, J. Huang, J. Mao, Q. Guo, Z. Chen and Y. Lai, *J. Mater. Chem. A*, 2020, **8**, 2934–2961.
34 H. Peng, F. Liu, X. Liu, S. Liao, C. You, X. Tian, H. Nan, F. Luo, H. Song, Z. Fu and P. Huang, *ACS Catal.*, 2014, **4**, 3797–3805.
35 J.-M. Yi, D. Wang, F. Schwarz, J. Zhong, A. Chimeh, A. Korte, J. Zhan, P. Schaaf, E. Runge and C. Lienau, *ACS Photonics*, 2019, **6**, 2779–2787.
36 C. Tian, D. Jiang, B. Li, J. Lin, Y. Zhao, W. Yuan, J. Zhao, Q. Liang, S. Gao, J. Hou and J. Qin, *ACS Appl. Mater. Interfaces*, 2014, **6**, 2162–2166.
37 X. Wan, J. Liu and J. Zhang, *Small Struct.*, 2022, **3**, 2200045.
38 Z. Peng, S. C. Abbas, J. Lv, R. Yang, M. Wu and Y. Wang, *Int. J. Hydrogen Energy*, 2019, **44**, 2446–2453.
39 S. Zhang, Z. Liu, M. Ruan, Z. Guo, L. E, W. Zhao, D. Zhao, X. Wu and D. Chen, *Appl. Catal., B*, 2020, **262**, 118279.
40 R.-B. Wei, P.-Y. Kuang, H. Cheng, Y.-B. Chen, J.-Y. Long, M.-Y. Zhang and Z.-Q. Liu, *ACS Sustain. Chem. Eng.*, 2017, **5**, 4249–4257.
41 C. Li, S. Chen, Y. Wang and Z. Hou, *Int. J. Hydrogen Energy*, 2019, **44**, 25416–25427.

42 K. Karmakar, A. Sarkar, K. Mandal and G. G. Khan, *Nanotechnology*, 2017, **28**, 325401.
43 S. Xie, W. Wei, S. Huang, M. Li, P. Fang, X. Lu and Y. Tong, *J. Power Sources*, 2015, **2977**, 9–15.
44 D. Maity, K. Karmakar, D. Pal, S. Saha, G. G. Khan and K. Mandal, *ACS Appl. Energy Mater.*, 2021, **4**, 11599–11608.
45 X.-S. Xing, X. Ren, X. Zeng, A. Li, Y. Wang, Z. Zhou, Y. Guo, S. Wu and J. Du, *Sol. RRL*, 2023, **7**, 2201041.
46 L. He, Z. Cui, X. Sun, J. Zhao and D. Wen, *Nanomaterials*, 2022, **12**, 2370.
47 S. Chang, H. Gu, H. Zhang, X. Wang, Q. Li, Y. Cui and W.-L. Dai, *J. Colloid Interface Sci.*, 2023, **644**, 304–314.
48 Z. Zhou, S. Wu, L. Qin, L. Li, L. Li and X. Li, *J. Mater. Chem. A*, 2018, **6**, 15593–15602.
49 X. Xiong, J. Zhang, C. Chen, S. Yang, J. Lin, J. Lin, J. Xi and Z. Kong, *J. Alloys Compd.*, 2022, **926**, 166863.
50 M.-W. Kim, B. Jishi, E. Samuel, H. Samuel, H. Seok, A. Aldabahi, M. Almoiqli, M. T. Swihart and S. S. Yoon, *Appl. Catal., B*, 2020, **271**, 118928.
51 L. Sun, J. Sun, X. Sun, S. Bai, Y. Zhao, R. Luo, D. Li and A. Chen, *J. Colloid Interface Sci.*, 2022, **608**, 2377–2386.
52 X.-S. Xing, M. Bao, P. Wang, X. Wang, Y. Wang and J. Du, *Appl. Surf. Sci.*, 2022, **572**, 151472.